

Article

Impact of Interaction between Metropolitan Area and Shallow Lake on Daily Extreme Precipitation over Eastern China

Zhe Li ^{1,2}  and Yanhong Gao ^{3,4,*} 

¹ Key Laboratory of Land Surface Process and Climate Change in Cold and Arid Regions, Northwest Institute of Eco-Environment and Resources, Chinese Academy of Sciences, Lanzhou 730000, China; lizheatm@lzb.ac.cn

² University of Chinese Academy of Sciences, Beijing 100049, China

³ Institute of Atmospheric Sciences, Department of Atmospheric and Oceanic Sciences, Fudan University, Shanghai 200438, China

⁴ Shanghai Frontiers Science Center of Atmosphere-Ocean Interaction, Fudan University, Shanghai 200438, China

* Correspondence: gaoyh@fudan.edu.cn

Abstract: Both cities and lakes have significant impacts on regional precipitation. With global warming, extreme precipitation events in Eastern China have increased significantly, and the single/joint influences of metropolises and lakes on extreme precipitation still need to be quantitatively evaluated. To reveal the impact of the single/joint influences of metropolises and lakes on the shear line torrential rain process, the Suzhou-Wuxi-Changzhou Metropolitan Area (SXCMA) and Lake Taihu in Eastern China were selected as the study area. Utilizing a WRF model, comparative studies of sensitivity simulations were conducted for the two typical extreme precipitation events caused by the low-level shear line (LLSL) on 27 June 2015 (EP627) and 25 September 2017 (EP925). Both results show that the existence of Lake Taihu and SXCMA will increase precipitation in the study area. SXCMA has a more obvious effect on enhancing precipitation, which is about twice the effect of Lake Taihu. SXCMA mainly strengthens the intensity and movement of the surface convergence line (SCL) in the study area and indirectly affects the shift of the LLSL, which finally affects the intensity and location of precipitation. Lake Taihu affects the intensity and movement of SCL, triggering ground vertical convections due to lower surface roughness, and acts as a land-lake breeze and water vapor source, which will affect the distribution and intensity of precipitation.

Keywords: extreme precipitation; metropolitan area; shallow lake



Citation: Li, Z.; Gao, Y. Impact of Interaction between Metropolitan Area and Shallow Lake on Daily Extreme Precipitation over Eastern China. *Atmosphere* **2022**, *13*, 306. <https://doi.org/10.3390/atmos13020306>

Academic Editors: Lei Meng and Yaqian He

Received: 10 January 2022

Accepted: 9 February 2022

Published: 11 February 2022

Publisher's Note: MDPI stays neutral with regard to jurisdictional claims in published maps and institutional affiliations.



Copyright: © 2022 by the authors. Licensee MDPI, Basel, Switzerland. This article is an open access article distributed under the terms and conditions of the Creative Commons Attribution (CC BY) license (<https://creativecommons.org/licenses/by/4.0/>).

1. Introduction

As of 2018, China has an urban population of 837 million, making it the most populous country in the world and accounting for about 20% of the global urban population. By 2050, China's urban population may increase by 255 million [1]. With the continuous growth of the urban population and the rapid expansion of urbanization, the impact of urbanization on regional weather and climate has become increasingly prominent, especially the changes in the temporal and spatial distribution of precipitation, which cannot be ignored.

The analysis of a large number of observations and numerical simulations in the past shows that cities have a significant impact on the precipitation intensity and location in an urban area [2–6], among which a considerable part of the research results found that precipitation in the leeward increases and proposed the following possible mechanisms: The thermal properties of the underlying surface of the city will produce unstable atmospheric conditions, which will affect the generation, intensification, and displacement of the mesoscale circulation [7]. Increased urban surface roughness enhances surface convergence [8]. Urban buildings block and divide the transit weather system [9]. Urban

irrigation and industrial activities increase the water vapor content of the lower atmosphere [10]. Cities change cloud microphysical processes by providing abundant sources of cloud condensation nuclei and increasing aerosol concentration [11].

Relative to other land surface classifications, a lake has a smaller albedo, lower surface roughness, and higher heat capacity. In addition, lakes also provide sufficient water vapor for the lower atmosphere [12]. Therefore, the lake–atmosphere interaction is significantly different from other land–atmosphere interactions in terms of the regional water cycle and energy budget and affects the weather and climate around the lake area [13–16]. Previous studies have shown that lakes can enhance the precipitation in the downwind area, which is called lake-effect precipitation [17–20]. This phenomenon not only occurs in large and deep lakes, but also in small and medium-sized lakes [21,22]. In addition, lakes will also affect the movement and intensity of the transit weather system, which will lead to changes in the temporal and spatial distribution of precipitation [23–25].

In Eastern China, dense cities and numerous lake–river networks coexist. For lakeside cities, the interaction between the urban heat island effects and the lake–land breeze circulation makes the precipitation mechanism more complicated [26,27]. Lake Taihu, located in southern Jiangsu Province, is the third largest freshwater lake in China, with an area of about 2400 km², which is deeper (2.5 m) in the west and north and shallower (<1.5 m) in the east, with an average depth of about 1.9 m [28]. In the past few decades, the Lake Taihu Basin has experienced rapid urbanization. The Suzhou-Wuxi-Changzhou Metropolitan Area (SXCMA) adjacent to Lake Taihu has a total population of 21.95 million, accounting for 28% of the total population of Jiangsu Province, and their GDP (Gross Domestic Product) is 378.6 billion yuan, accounting for 40% of Jiangsu's total GDP, which is an important part of the population and economy in the Yangtze River Delta urban agglomeration [29]. Previous studies have shown that the temperature difference between Lake Taihu and the surrounding land will form conspicuous lake–land breeze circulation, which will affect the weather/climate conditions of the surrounding area [30–32].

Studies have shown that climate change will potentially increase the frequency and intensity of extreme precipitation [33]. Per degree of increase in China due to global warming, heavy rainfall events are expected to increase by 6.52% (5.22–8.57%) [34], and global warming has been thought to be the main factor that has caused the increase in heavy rainfall in Eastern China [35]. Furthermore, extreme precipitation events in the middle and lower reaches of the Yangtze River also showed a significant increase [36,37]. Peng et al. evaluated extreme precipitation events in China in the past 58 years (1960–2017) and in the future (2011–2100) based on observations and Coupled Model Intercomparison Project Phase 5 (CMIP5) projections, finding that the precipitation amount and the extreme precipitation index in southeastern China show an increasing trend in both historical and future stages. Zhang et al. found that the location and intensity of the Western Pacific Subtropical High (WPSH) has a significant impact on the extreme precipitation in Eastern China [38], and the combined effects of the WPSH and the South Asian High will lead to continuous extreme precipitation events [39]. Typhoons, Meiyu fronts, and low-level vortex/shear line have made considerable contributions to extreme precipitation events in the lower reaches of the Yangtze River [40,41]. Gao and Xie analyzed data from meteorological stations in the Yangtze River Basin from 1960 to 2011 and found that stations with a significant upward trend were mainly located in the mainstream and tributaries, as well as near large lakes [42]. Liu et al. analyzed the observation data of meteorological stations in Eastern China, finding that during 1955–2011, the heavy rainfall in both rural and urban stations increased significantly [35]. Kang et al. analyzed the extreme precipitation index using meteorological observation data from 1980 to 2015, and the results show that the extreme precipitation intensity index of the SXCMA shows an upward trend, indicating that urbanization will increase extreme precipitation [43]. In recent years, increasing studies have shown that Lake Taihu and the surrounding SXCMA are experiencing increasing extreme precipitation events.

With the rapid progress of urbanization and the increase of extreme precipitation events against the background of climate change, the impact of Lake Taihu and SXCMA on extreme precipitation cannot be ignored. However, there is little research in this field as to whether there is any interaction between the Lake Taihu and the SXCMA in the process of extreme precipitation, and how much the impact on the regional precipitation can be, which are topics worthy of discussion and study. In this study, experiments were designed to analyze the single or joint impact of metropolises and lakes in Eastern China. Section 2 describes the extreme events, datasets, model configurations, and experiments. Results are included in Section 3 in terms of the validations of the control runs, the comparisons between sensitive runs and control runs, and the mechanisms. Section 4 concludes and discusses.

2. Materials and Methods

2.1. Two Extreme Precipitation Events

The shear line is one of the main weather systems that triggers precipitation over the Yangtze-Huaihe River area. Ma et al. found that the number of shear line torrential rain days in the Yangtze-Huaihe River area from June to July of 1981–2013 accounted for nearly 75% of the rainstorm days [44], so the shear line is closely related to the occurrence of torrential rain. Based on the daily precipitation of three meteorological stations in Wuxi, Changzhou, and Suzhou from 2014 to 2018, taking the 99th percentile daily precipitation amount as the extreme precipitation threshold, the 27 June 2015 (EP627) and 25 September 2017 (EP925) precipitation events caused by low-level shear line (LLSL) were selected as the examples of extreme precipitation events in this study.

EP627: The torrential rain occurred on 27 June 2015, when the 500 hPa WPSH extended westward and northward along with a westerly trough on the east coast of China, and the shear line occurred on 850 hPa over the Yangtze-Huaihe River area. Affected by the above system, a torrential rain belt (>100 mm) appeared in the central part of Anhui Province to the southern part of Jiangsu Province (Figure 1a–c). The center of the torrential rain appeared in the Jiangnan area of southern Jiangsu Province. Rainfall of more than 200 mm happened at several meteorological stations.

EP925: The torrential rain occurred on 25 September 2017. The 500 hPa WPSH intensified and extended westward. Visible westerly troughs existed in southwest China, along with LLSLs and jets. Against the background of the above circulation, torrential rain occurred in the southern part of the Huanghuai area, the northern and Eastern Yangtze-Huaihe River area, and the northeastern Jiangnan area. On the 24th, torrential rain was concentrated in southern Jiangsu Province, Shanghai, and northern Anhui Province. Heavy rain (>50 mm) appeared at 63 meteorological stations, 13 of which showed torrential rain (>100 mm). On the 25th, Heavy rain occurred at 43 meteorological stations in southern Jiangsu Province and Shanghai, 11 of which displayed torrential rain (Figure 2a–c).

The two extreme precipitation events induced severe floods of local rivers, lakes, and parts of farmland, traffic interruption, and urban waterlogging, which caused considerable economic losses. Therefore, research on this type of extreme precipitation can provide a further understanding of the role of SXCMA and Lake Taihu in the torrential rain process, which will help improve the model's ability to predict similar torrential rain disasters and improve the level of disaster prevention and mitigation.

2.2. Model Configuration

Weather Research and Forecasting (WRF), as a fully compressible and nonhydrostatic mesoscale weather forecast model, is widely used in the fine research of meso- and small-scale weather systems. WRF version 3.8.1 was used in this study. Considering the impact of the Tibetan Plateau on precipitation in east China [45], the model uses two-way four-fold nesting, and the outermost grid includes the entire Tibetan Plateau, with grid resolutions of 27, 9, 3, and 1 km. To account for the limitation of computing resources, the model is divided into 30 layers in the vertical direction, and the number of horizontal grid points

are 207×165 , 238×334 , 508×640 , and 895×868 . The specific locations of the domains are shown in Figure 3a.

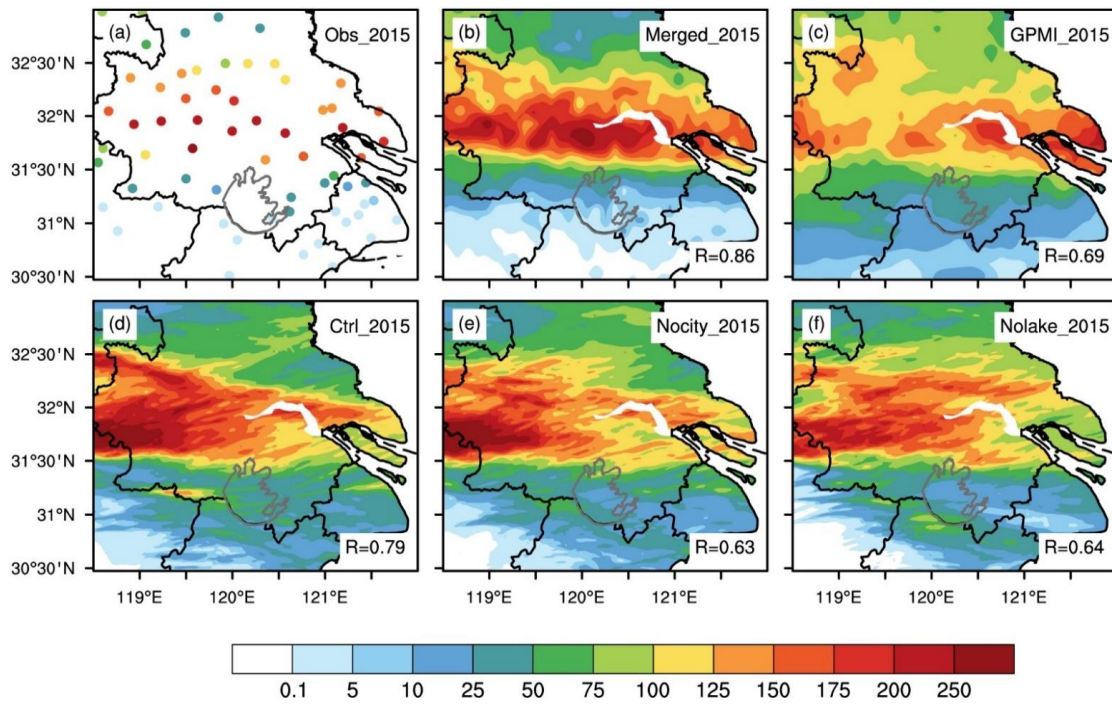


Figure 1. The distributions of the daily precipitation (unit: mm) for (a) the station observations, (b) the Merged, (c) the GPMI and (d–f) three simulations (control, Nocity, and Nolake) for EP627. The right-bottom R denotes the spatial correlation coefficients between the observation and the corresponding dataset.

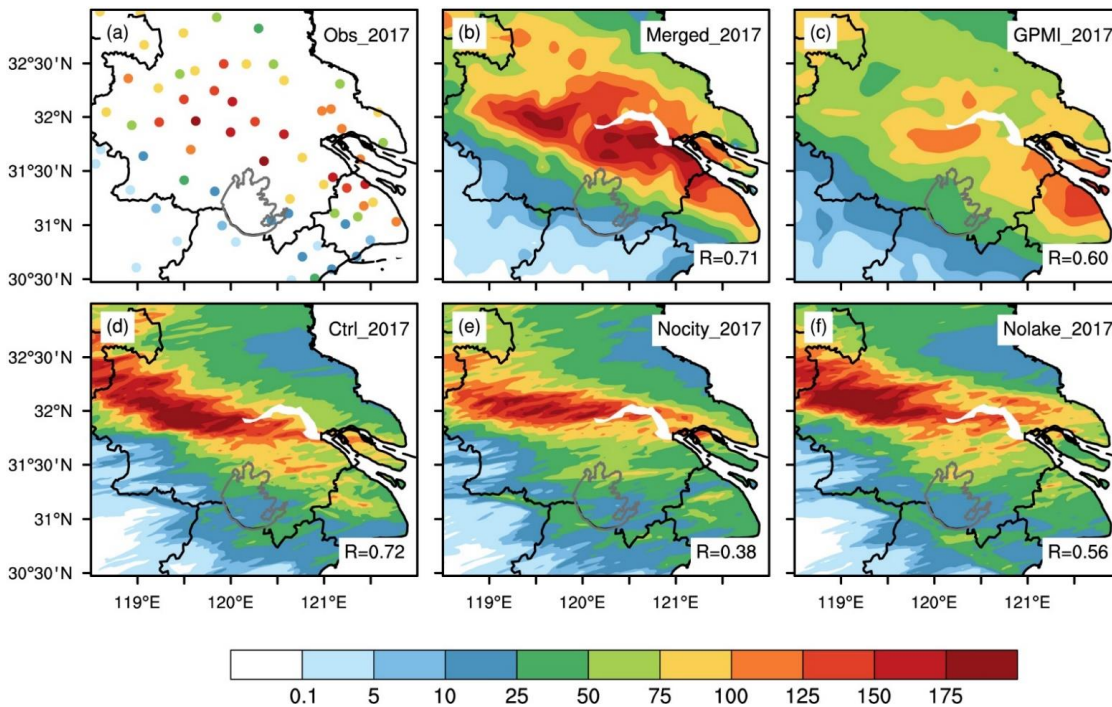


Figure 2. The distributions of the daily precipitation (unit: mm) for (a) the station observations, (b) the Merged, (c) the GPMI and (d–f) three simulations (control, Nocity, and Nolake) for EP925. The right-bottom R denotes the spatial correlation coefficients between the observation and the corresponding dataset.

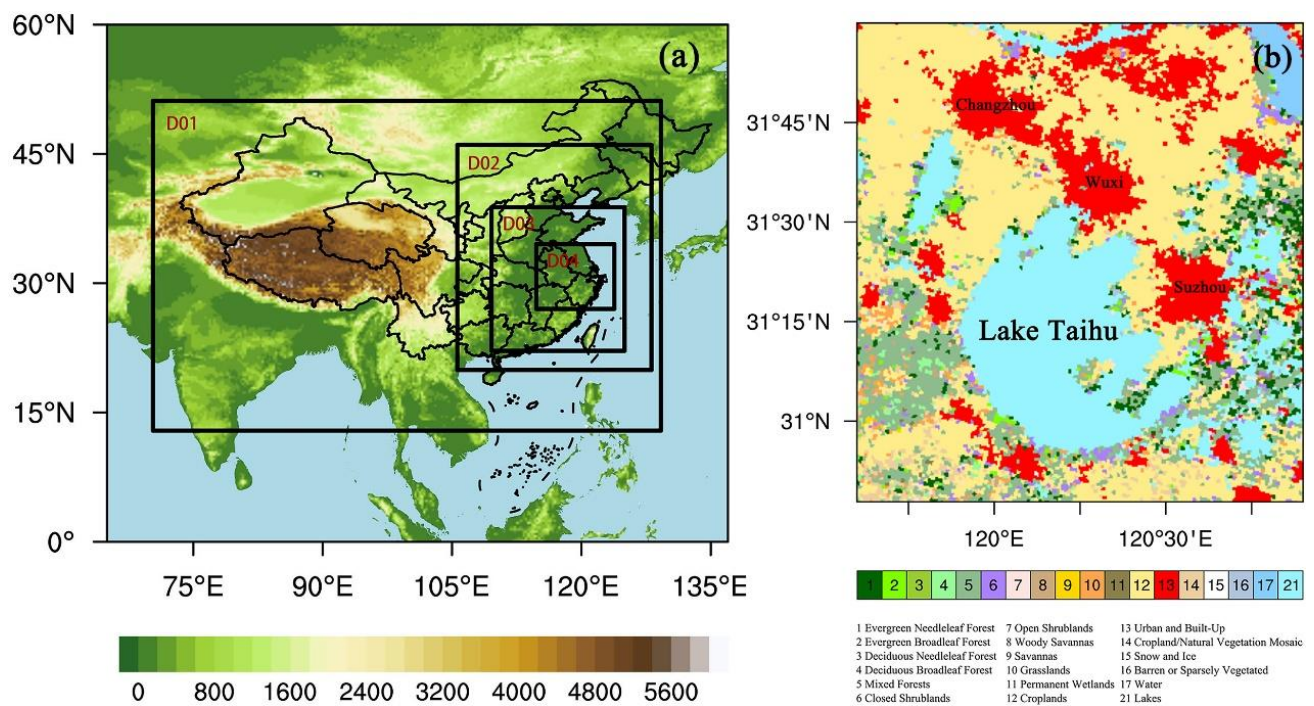


Figure 3. (a) The domains for WRF simulations and the terrain height for the outer domain (unit: m); (b) The land use of study area, derived from the 20-category IGBP-Modified MODIS.

Per the impact of the parameterization combinations on simulation, commonly used microphysics, cumulus (used in 27 km and 9 km), boundary layer, and longwave and shortwave radiation parameterization schemes were used for the high-resolution simulation in Eastern China [46–51]. Combinations of eight microphysics schemes (Lin, WSM5, WSM6, Goddard, Thompson, Morrison 2-mom, WDM6, and NSSL 2-mom), two boundary layer schemes (YSU and MYJ), two cumulus schemes (Kain-Fritsch and Grell-Devenyi), four longwave and shortwave radiation schemes (RRTM, Dudhia, CAM, and RRTMG), and the Noah-MP land surface scheme are performed and evaluated with the observed precipitation. The optimal combination of the WSM6 microphysical scheme, RRTM longwave radiation scheme, Dudhia short-wave radiation scheme, MYJ planetary boundary layer scheme, Kain-Fritsch cumulus convection scheme (turned off for the domain 3 and 4), Noah-MP land surface scheme was selected and used in the control run.

ERA-Interim with a time interval of 6 h was used as the forcing. The lake model in WRF 3.8.1 [52] was turned on. The simulation period of EP627 is from 02:00 LST on 26 June to 20:00 LST on 27 June 2015. The first 18 h was taken as spin-up time. The simulation period of EP925 is from 08:00 LST on 24 September to 20:00 LST on 25 September 2017. The first 12 h is the spin-up time. The output interval is one hour.

2.3. Experiments

Besides the control run (Figure 3b), two sensitivity simulations were designed for EP627 and EP925. The first replaces SXCMA in the control simulation with the land use type of the nearest grid cell, which is named Nocity in the following. The second replaces the entirety Lake Taihu in the control simulation with the land use type of the nearest grid cell, which is named Nolake in the following. The rest remains the same as in the control run.

2.4. Observation Data

Four type observation data sets are used:

- (1) S-band raw radar data of CINRAD-SA Doppler weather radar in Changzhou (119.780° E, 31.901° N), Jiangsu.

- (2) Observation data of national hourly automatic rain gauge stations.
- (3) China’s automatic stations and CMORPH (Climate Prediction Center MORPHing technique) merged the hourly precipitation grid data set (Merged) provided by the China Meteorological Data Service Centre. The data set integrates the hourly precipitation of more than 30,000 automatic observation stations across China with the real-time satellite precipitation products retrieved by CMORPH, producing the merged data with a spatial resolution of 0.1° and a temporal resolution of per hour, which has a high accuracy in China, as well as captures the main changes of hourly precipitation during heavy precipitation [53].
- (4) The Global Precipitation Measurement (GPM) Integrated Multi-satellite Retrievals for GPM (IMERG) Final Precipitation L3 Half Hourly 0.1-degree × 0.1-degree V06 (GPMI) [54]. The data set applies the unified algorithm that provides rainfall estimates by combining data from all of the passive-microwave instruments in the GPM Constellation, performs well in the lower reaches of the Yangtze River [55], and has a better capture of the actual variation tendency of hourly precipitation in extreme precipitation events [56].

The nearest neighboring grid cells to the station sites are used in the evaluation with the station records. We focus on the daily amount, locations, and hourly propagation of the extreme precipitation belts. The spatial correlation coefficients between the Merged, the GPMI, and the station observation data were used to detect the similarity of the precipitation pattern between the observations and the Merged or GPMI.

2.5. Forecast Skill Scores

To verify the quantitative precipitation forecast of the model based on the total numbers of observed and forecasted occurrences and non-occurrences of the contingency table under a selected threshold (Table 1), the statistical results are divided into four categories: hits (*a*), false alarms (*b*), misses (*c*), correct negatives (*d*). The four types of skill scores are computed from the contingency table [57]; Bias Score (*BIAS*) measures the ratio of the frequency of forecasted events to the frequency of observed events (perfect score = 1). Threat Score (*TS*) measures the fraction of observed events that were correctly predicted (perfect score = 1). Equitable Threat Score (*ETS*) is *TS* adjusted for hits associated with random chance (perfect score = 1). True Skill Statistic (*TSS*) uses all elements in the contingency table to give an overall assessment of the forecast (perfect score = 1). The equations of those scores are as follows:

$$BIAS = \frac{a + b}{a + c} \tag{1}$$

$$TS = \frac{a}{a + b + c} \tag{2}$$

$$a_r = \frac{(a + b)(a + c)}{a + b + c + d} \tag{3}$$

$$ETS = \frac{a - a_r}{a + b + c - a_r} \tag{4}$$

$$TSS = \frac{a}{a + c} - \frac{b}{b + d} \tag{5}$$

Table 1. A contingency table of forecast and observation events for a selected threshold.

Observation	Forecast	
	Yes	No
yes	a	c
no	b	d

3. Results

3.1. Control Run Evaluations

3.1.1. EP627

The EP627 station observation shows that the large precipitation event is mainly distributed the north of Lake Taihu. The pattern correlation coefficients of daily precipitation between the observations and the Merged, GPMI, and three simulations all passed the significance test of $\alpha = 0.01$. The correlation between the control run and the observation is 0.79, which ranks second, behind the Merged and even higher than GPMI (Figure 1d). The correlation coefficients of daily precipitation between Nocity and observations and Nolake and observations are 0.63 and 0.64, respectively (Figure 1e,f). In terms of the capability of torrential rain forecasting (≥ 50 mm), the control run has a lower BIAS and higher TS, ETS, and TSS than Nocity and Nolake (Table 2), presenting the best forecast skill.

Table 2. The skill scores of torrential rain (≥ 50 mm) in the control, Nocity, and Nolake runs for two events.

	2015			2017		
	Ctrl	Nocity	Nolake	Ctrl	Nocity	Nolake
BIAS	1.08	1.12	1.17	0.70	0.58	0.62
TS	0.83	0.76	0.77	0.70	0.58	0.62
ETS	0.67	0.56	0.56	0.47	0.35	0.39
TSS	0.80	0.71	0.71	0.70	0.58	0.62

Among the four curves of the diurnal variation of the average hourly accumulated precipitation within the study area (Figure 4a), the Merged is closest to the observation data. The control run is similar to the observation data, but the curve is steeper than that of the observation. The curve of GPMI differs greatly from the observation data. On the whole, the control run basically expresses the spatial distribution and temporal changes of the extreme precipitation process in the study area.

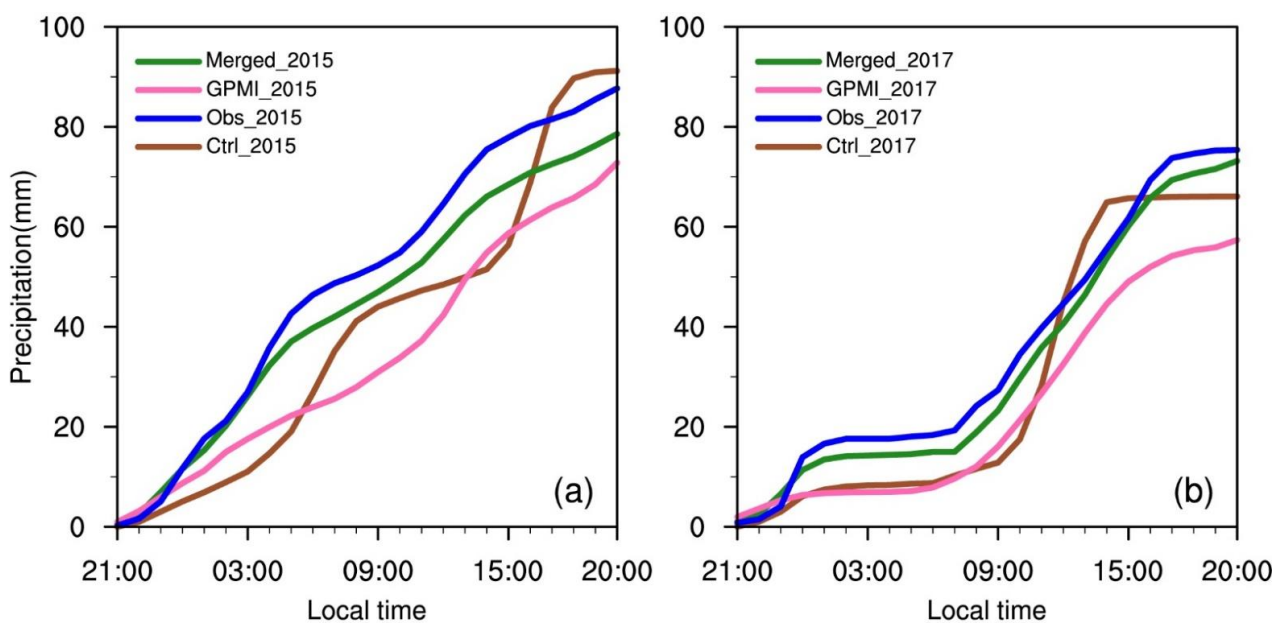


Figure 4. A comparison of the observation, GPMI, Merged, and simulated hourly accumulated precipitation averaged over the study area for (a) EP627 and (b) EP925.

From the composite reflectivity detected by the radar, it is known that the shear line is located near Changzhou at 15:01 and starts to intrude into the study area, then arrives

in Wuxi at 16:01, and finally moves to Suzhou at 17:00 (Figure 5a1–a3). The control run simulation generally follows the radar-detected the position of the shear line, but with a slightly higher intensity than the observation (Figure 5b1–b3).

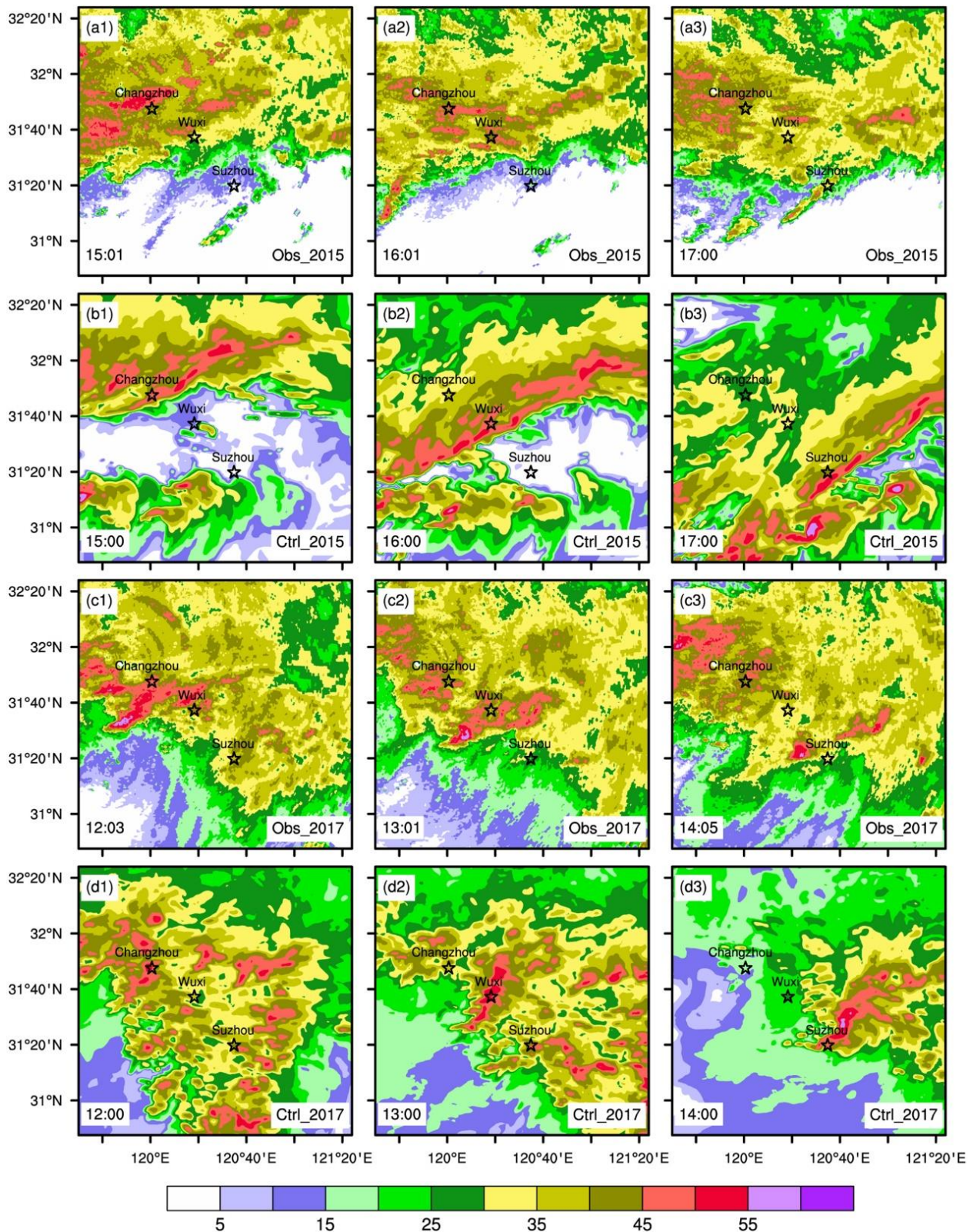


Figure 5. The distributions of (a1–a3) radar composite reflectivity and (b1–b3) simulated composite radar reflectivity (unit: dBZ) for EP627. (c1–c3,d1–d3) is the same as (a1–a3,b1–b3), but for EP925.

3.1.2. EP925

EP925 shows the center of precipitation located north of Lake Taihu, where 10 stations accumulated precipitation of more than 100 mm. As in EP627, the pattern correlation coefficients between the observation and the Merged, GPML, and three simulations all pass the significance test of $\alpha = 0.01$. The two sensitivity runs (Nocity and Nolake) have a low spatial correlation with observed precipitation, only 0.38 and 0.56 (Figure 2e,f), indicating that the distribution of 24 h of accumulated precipitation changed greatly. As for the skill scores of torrential rain, the control run shows the best forecasting skill among all three experiments, with the lowest BIAS and top TS, ETS, and TSS (Table 2).

For the diurnal variation of the average hourly accumulated precipitation within the study area (Figure 4b), the Merged is the closest to the observation data. The curves of the control run and the observation data are relatively similar, although there are some differences to the observation data, which exhibit better results than GPML in the hourly precipitation propagations. In general, the control run can basically reflect the overall precipitation spatial distribution and the variations in hourly precipitation in the study area.

The composite reflectivity exhibits that the shear line passes through Changzhou, Wuxi, and Suzhou at 12:03, 13:01, and 14:05, respectively (Figure 5c1–c3). In the control run, the position of the shear line at the corresponding time is quite close to radar observation, but a little stronger than observation (Figure 5d1–d3).

Both events illustrate that although it can discern the large-value area of 24 h accumulated precipitation, GPML does not perform as well in the overall distribution of accumulated precipitation intensity as Merged. This indicates that the Merged is better at capturing the precipitation amount and the propagation of these two precipitation processes than the GPML, which may be due to the different data sources and methods for data generation.

3.2. Precipitation Differences between Sensitive Runs and Control Run

3.2.1. EP627

Large precipitation concentrates in the two areas of Changzhou and Wuxi and centers near Changzhou, which reaches up to 180 mm in the control run (Figure 6a1). For Nocity, the precipitation at SXCMA is less than that of the control run, and the difference is about 20–50 mm (Figure 6a4). The area of the precipitation center is relatively smaller and to the south of the one in the control run (Figure 6a2). For Nolake, the precipitation concentration zone is similar to the control run (Figure 6a3) but with smaller magnitudes (Figure 6a5). The Nocity and Nolake simulations produce 10.6% and 5.8% less precipitation than the control run, respectively (Table 3).

Table 3. A comparison of the simulated daily precipitation (units: mm) for the control and two sensitive runs and the relative biases in the sensitive runs compared to the control run for two events.

	EP627	EP925
Ctrl	91.2	66.1
Nocity	81.5	55.6
Nolake	85.9	61.3
(Nocity-Ctrl)/Ctrl	−10.6%	−15.9%
(Nolake-Ctrl)/Ctrl	−5.8%	−7.3%

In the hour with the most intense precipitation in the study period(15:00–16:00), a large precipitation concentration zone shows in the southeast area of Changzhou (Figure 6b1), with a central intensity of about 55 mm. The Nocity run shows the rain belt to the north of Changzhou (Figure 6b2). The Nolake run shows an apparent precipitation center in northern Changzhou (Figure 6b3), and its intensity is close to that of the control run. Both

sensitive runs show less precipitation than that of the control run in the southern part of Changzhou (Figure 6b4,b5).

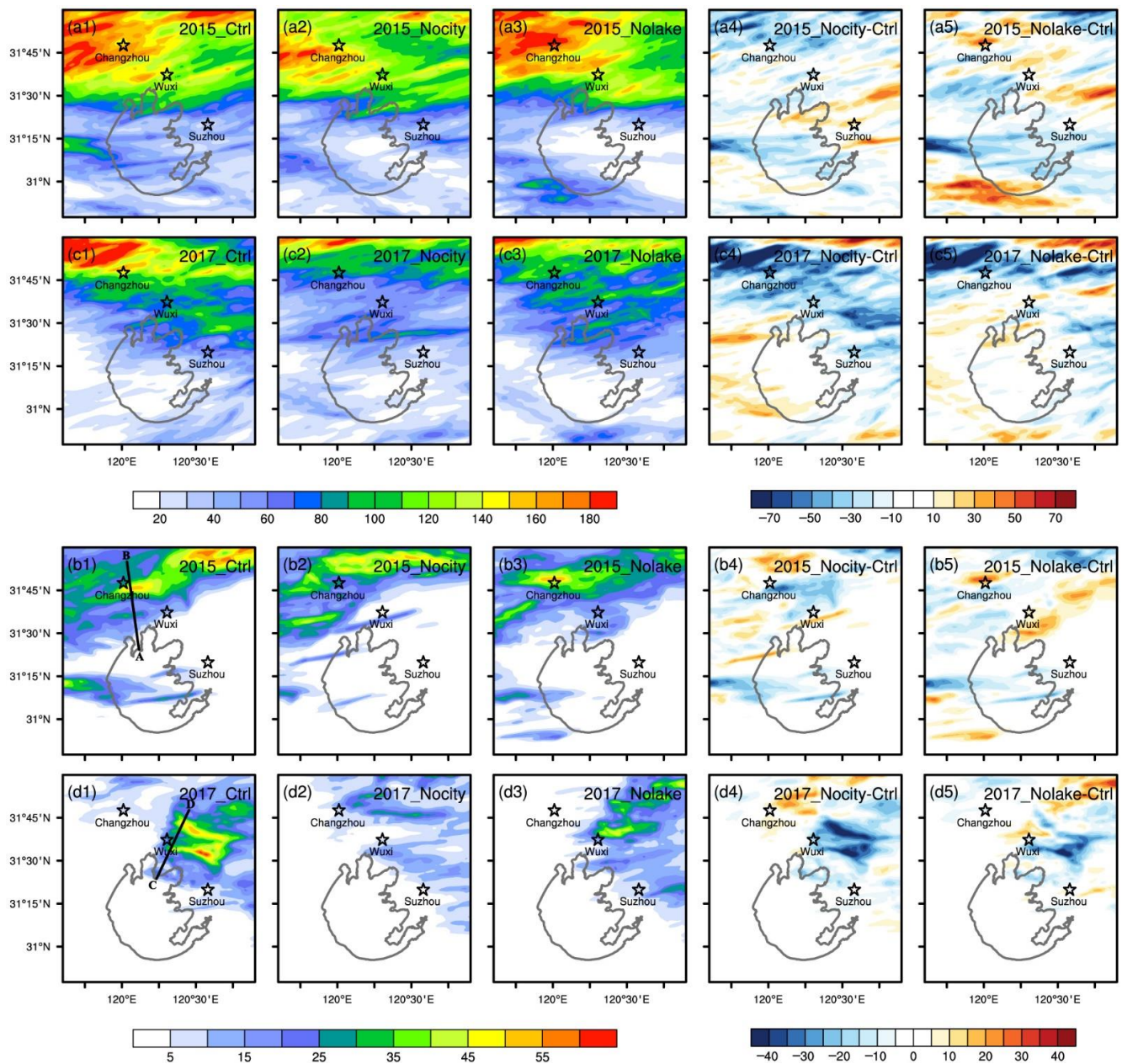


Figure 6. The distributions of the simulated daily precipitation (unit: mm) in the (a1) control and (a2,a3) two sensitive (Nocity and Nolake) runs for EP627, as well as (a4,a5) the differences between the sensitive runs and the control run. (c1–c5) are the same as (a1–a5), but for EP925. (b1–b5) and (d1–d5) are the same as (a1–a5), but for the maximum hourly precipitation which occurred from 15:00–16:00 for EP627 and from 13:00–14:00 for EP925. The line AB in (b1) and the line CD in (d1) are the cross sections used in the latter analyses.

3.2.2. EP925

The control run simulates a significant precipitation to the northwest of Changzhou, with an intensity of about 180 mm (Figure 6c1). The precipitation belts of the Nocity and Nolake runs locate to the north of that in the control run (Figure 6c2,c3), resulting in lower precipitation at SXCMA than in the control run (Figure 6c4,c5). According to the results of the statistical analysis, when considering the average 24 h accumulated precipitation in the

study area, the Nocity and Nolake runs have 15.9% and 7.3% less precipitation than the control run, respectively (Table 3).

The LLSL of EP927 passes through Changzhou, Wuxi, and Suzhou at 12:03, 13:01, and 14:05, respectively. The most intense precipitation occurs at Wuxi from 13:00–14:00. The control run produces visible precipitation near Wuxi (Figure 6d1), with a center intensity of about 55 mm. Nocity does not simulate a clear precipitation center around Wuxi (Figure 6d2). For Nolake, the range and intensity of the precipitation area near Wuxi are weaker than the control run (Figure 6d3). The difference in precipitation intensity shows that there is a large area of negative value around Wuxi between Nocity/Nolake and the control run (Figure 6d4,d5), and the central values reach about -40 mm/ -25 mm, respectively.

3.3. Differences in Surface Skin Temperature and Local Circulation

Taking the surface skin temperature (SKT) as a representative element of surface energy accumulation, we further analyzed the SKT one hour before the most intensive hourly precipitation induced by shear line.

3.3.1. EP627

The SKT of SXCMA at 14:00 is significantly higher than the surrounding environment, forming a high temperature zone in the control run (Figure 7a1). The SKT of SXCMA in Nocity is 2~3 °C lower than the control run (Figure 7a2). Nolake has a 3~4 °C higher temperature over the lake than the control run (Figure 7a3).

As the LLSL approaches the study area at 15:00, the near-surface wind forms evident high wind speed zones in Changzhou and Wuxi (Figure 7b1), and the high-speed center near Changzhou is as large as 15 m s⁻¹. At the same time, the surface convergence line (SCL) corresponding to the LLSL is generated near Changzhou (Figure 8a1) with an intensity of about -4×10^{-3} s⁻¹. For Nocity, the area of near-surface high wind speed and the SCL are formed in the northwest, outside Changzhou (Figures 7b2 and 8a2), and the range and intensity are distinctly weaker than the control run. Although the near-surface wind speed is higher in Nolake than in the control run in Changzhou (Figure 7b3), the wind speeds in Wuxi, Suzhou, and Lake Taihu are significantly lower than in the control run, with a difference of about 2~3 m s⁻¹. At the same time, the position of the SCL of Nolake is to the southeast of the control run (Figure 8a3), with little difference in intensity between the two.

From the cross-sectional view, the control run clearly produces a strong vertical circulation over Changzhou (Figure 9a1). The center intensity of the vertical ascending motion is about 4 m s⁻¹. The vertical circulation blocked the low-level water vapor transport from the south (Figure 9b1), causing the accumulation of water vapor and forming a large water vapor center of about 45 g s⁻¹ hPa⁻¹ cm⁻¹. When combined with Figure 6b1, it can be found that the center of the large value of water vapor flux also corresponds well to the location of the precipitation center in southern Changzhou. Nocity only forms a weak vertical ascending motion (~ 1 m s⁻¹) over Changzhou (Figure 9a2). Although an evident center of water vapor fluxes exists in the low level (Figure 9b2), no strong precipitation center forms in Changzhou due to a lack of vertical circulation (Figure 6b2).

Nolake produces two vertical circulations (Figure 9a3). The circulation on the south side originated from the vertical upward movement formed by the strong convergence of the ground, and the other circulation on the north side originated from the vertical ascending motion caused by the LLSL. The north one is obviously stronger, leading to more precipitation from the southern center of the water vapor fluxes (Figure 9b3). The precipitation zone is therefore significantly more northern than in the control run (Figure 6b3).

3.3.2. EP927

The SKT of Wuxi and Suzhou in the control run is higher than the surrounding environment by about 1 to 2 °C (Figure 7c1). The Nocity run is consistent with the surrounding environment (Figure 7c2), being 1~2 °C lower than the control run. The urban SKT of

Nolake is not much different from the control run (Figure 7c3), but the SKT in the northern half of Lake Taihu is about 1 °C lower than in the control run.

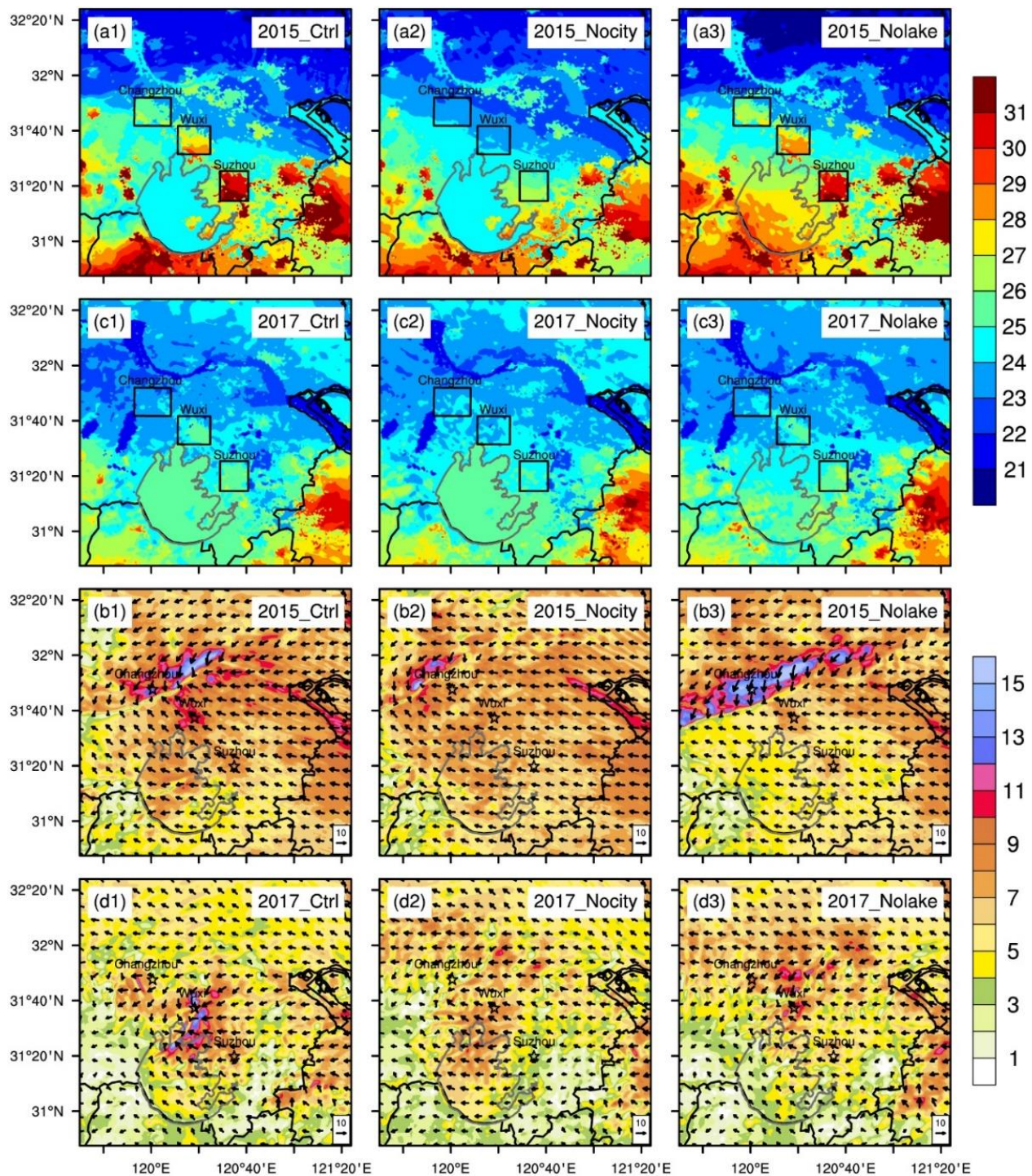


Figure 7. The spatial distributions of the simulated surface skin temperature (unit: °C) at one hour before the hour with the most intense precipitation, at (a1–a3) 14:00 in EP627 and at (c1–c3) 12:00 in EP925. (b1–b3) and (d1–d3) are the near-surface wind speed (unit: m s⁻¹) and the wind direction (the arrows) at the starting point of the hour with the most intense precipitation, at 15:00 in EP627 and at 13:00 in EP925. 1–3 denote the control and two sensitive (Nocity and Nolake) runs, respectively.

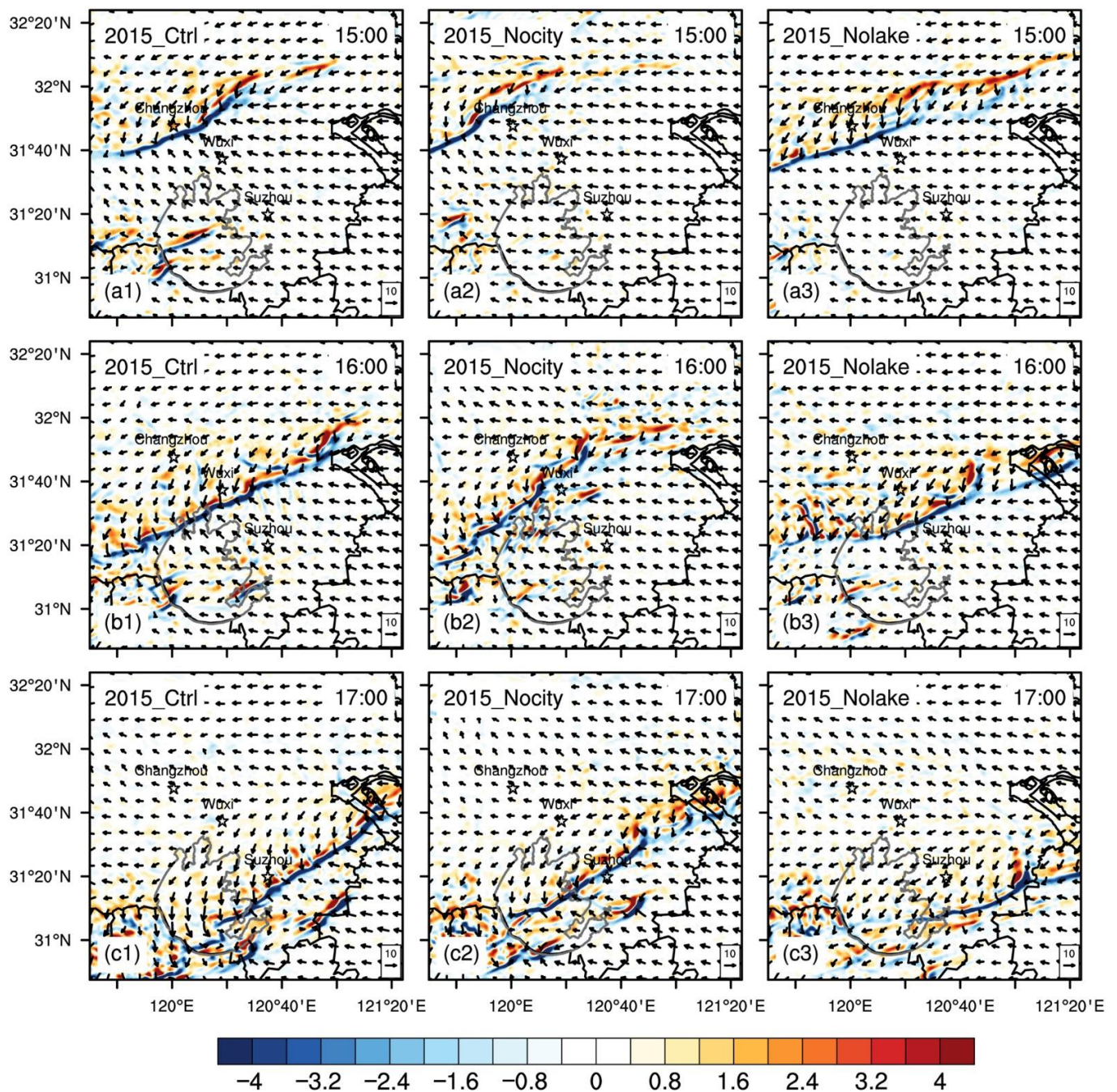


Figure 8. The spatial distributions of the near-surface wind direction and divergence (unit: 10^{-3} s^{-1}) for the (a1,b1,c1) control, (a2,b2,c2) Nocity, (a3,b3,c3) Nolake runs for EP627.

In the control run, LLSL is generated from Wuxi to the north side of Lake Taihu (Figure 7d1). A high wind speed center is formed in Wuxi, with an intensity of about 14 m s^{-1} . However, in Nocity, no clear wind speed center can be found (Figure 7d2). In Nolake, a high wind speed center in Wuxi is produced, but with a much lower intensity of only 10 m s^{-1} (Figure 7d3). Corresponding to the LLSL, the SCL is moving from Changzhou to Suzhou with a intensity of $-3.2 \times 10^{-3} \text{ s}^{-1}$ from 12:00–14:00 (Figure 10a1,b1,c1). By contrast, Nocity shows no explicit SCL (Figure 10a2,b2,c2), and Nolake is much weaker than the control run (Figure 10a3,b3,c3).

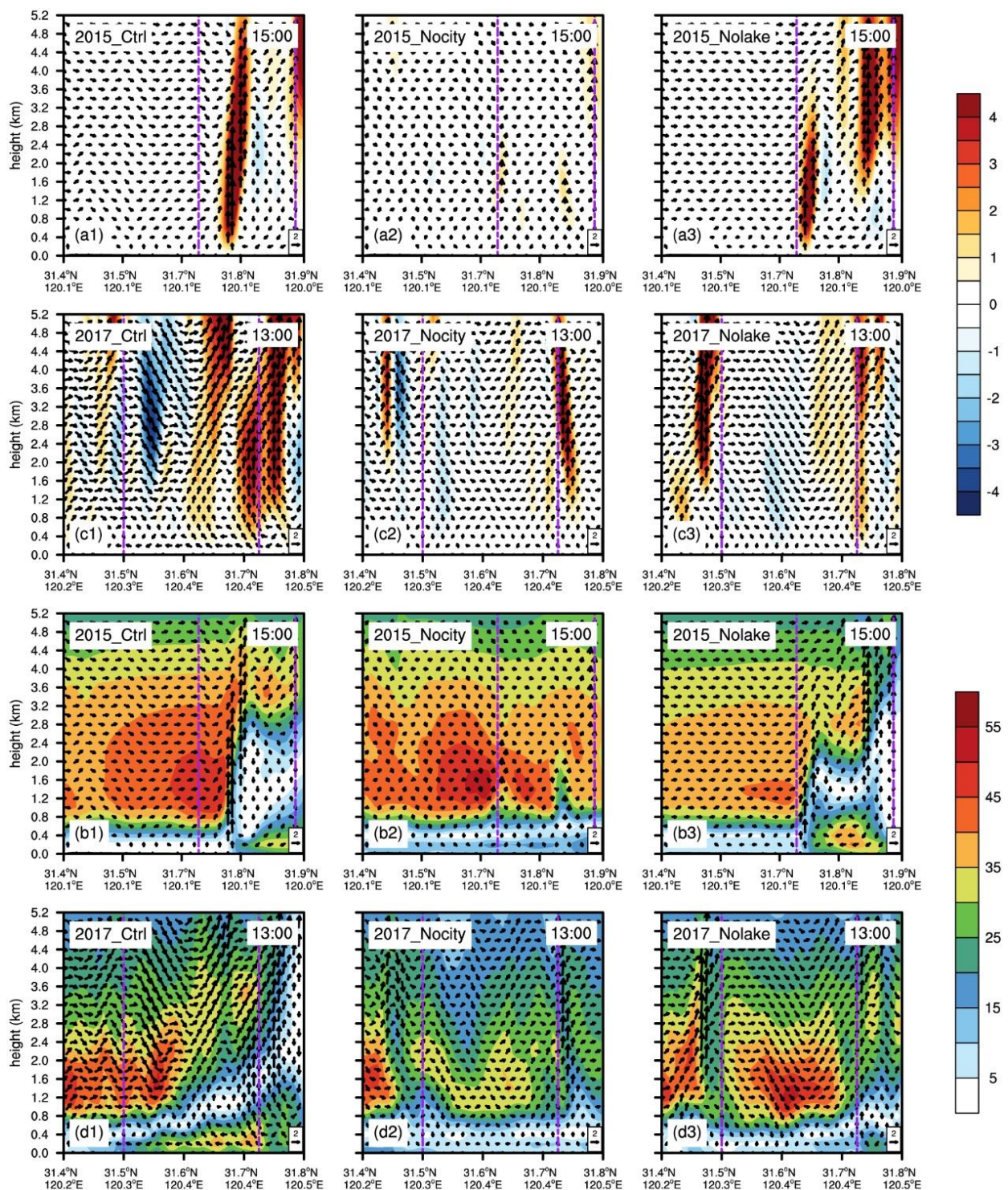


Figure 9. The cross sections of the (a1–a3) vertical velocity (unit: m s^{-1}) and (b1–b3) water vapor flux (unit: $\text{g s}^{-1} \text{hPa}^{-1} \text{cm}^{-1}$) at 15:00 along the AB in Figure 6b1 for EP627 in the (a1,b1) control, (a2,b2) Nocity, (a3,b3) and Nolake runs. (c1–c3,d1–d3) are the same as (a1–a3,b1–b3), but at 13:00 along the CD in Figure 6d1 for EP925. The urban area is marked between two dashed purple vertical lines.

Under the cross-sectional part, the control run has formed two conspicuous vertical upward movement zones in the urban area of Wuxi and near the northern edge of Wuxi, and two corresponding vertical circulations. The vertical circulation to the north is stronger (Figure 9c1), leading to the accumulation of water vapor on the south side of the circulation, and the two vertical circulations have an obvious water vapor flux center on the south

side (Figure 9d1), with intensities around 50 and $35 \text{ g s}^{-1} \text{ hPa}^{-1} \text{ cm}^{-1}$, respectively. There is a good corresponding relationship with the precipitation center of Figure 6d1. Nocity has no marked vertical upward movement in the urban area (Figure 9c2), and no vertical circulation is formed. Accordingly, no significant precipitation is produced (Figure 6d2). For Nolake, there is a weak vertical ascending movement at the northern edge of the urban area, and a vertical circulation is formed (Figure 9c3). A visible water vapor flux center is also shown on the south side of the vertical circulation (Figure 9d3). However, because the number and intensity of the vertical circulations are markedly weaker than in the control run, there is no significant precipitation in the urban area (Figure 6d3).

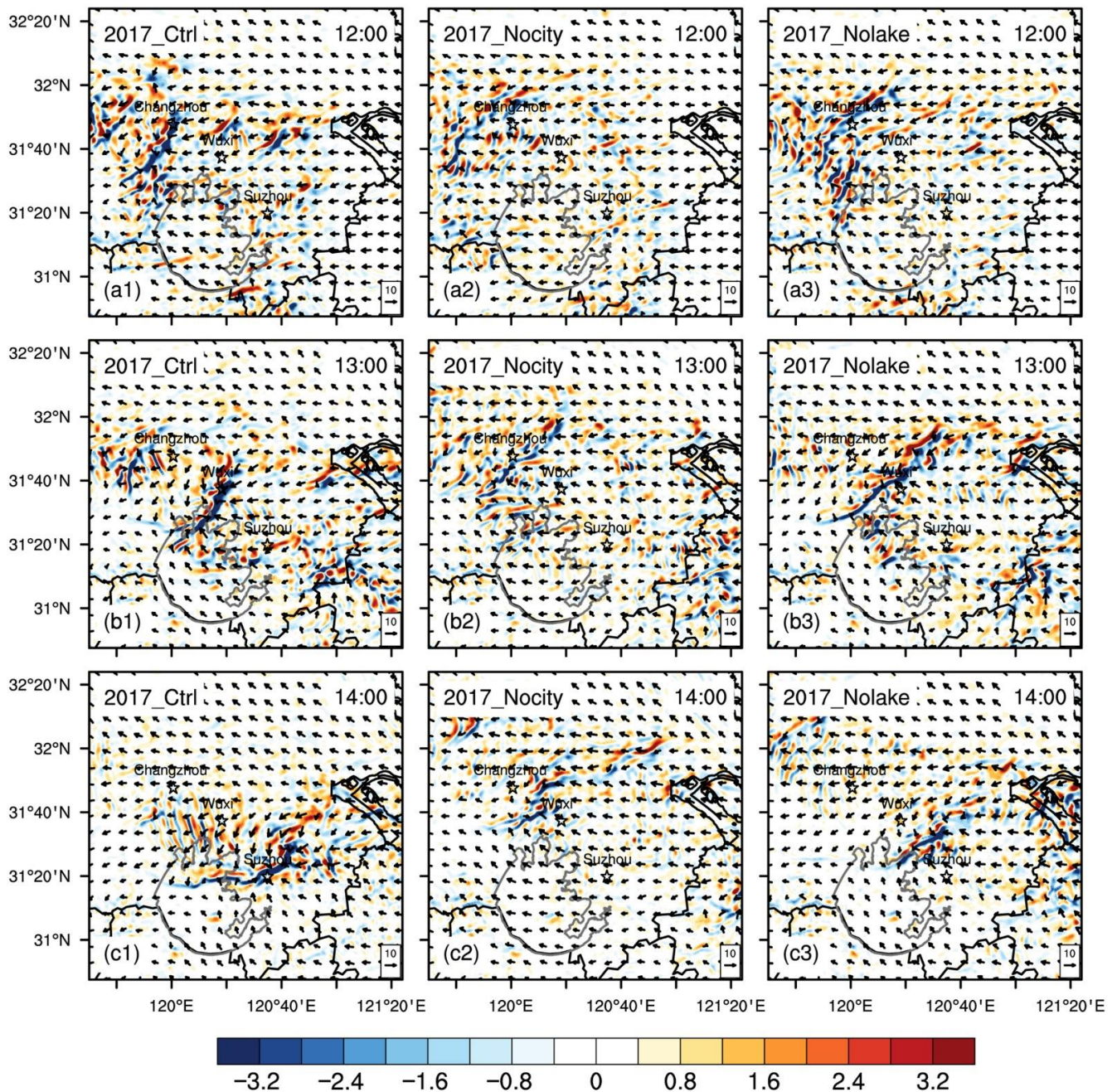


Figure 10. The spatial distributions of the near-surface wind direction and divergence (unit: 10^{-3} s^{-1}) for the (a1,b1,c1) control, (a2,b2,c2) Nocity, (a3,b3,c3) Nolake runs for EP925.

3.4. Differences of Shear Line and Water Vapor Propagation

3.4.1. EP627

Since the extreme precipitation is caused by the LLSL, we chose the movement of the 850 hPa shear line shift in the study area to explore the impact of SXCMA and Lake Taihu on the LLSL. In the control run (Figure 11a1,b1,c1), the 850 hPa shear line passes through Changzhou at 15:00, further intensifies to reach southeast of Wuxi at 16:00, and then gradually weakens and moves to the southeast of Suzhou at 17:00. The corresponding SCL (Figure 8a1,b1,c1) has the same moving direction and changing trend as the 850 hPa shear line, except that the SCL does not significantly weaken at 17:00. The difference between the two appears at 15:00. The position of the SCL is clearly to southeast of the 850 hPa shear line, but the positions of the two basically coincide at 16:00 and 17:00.

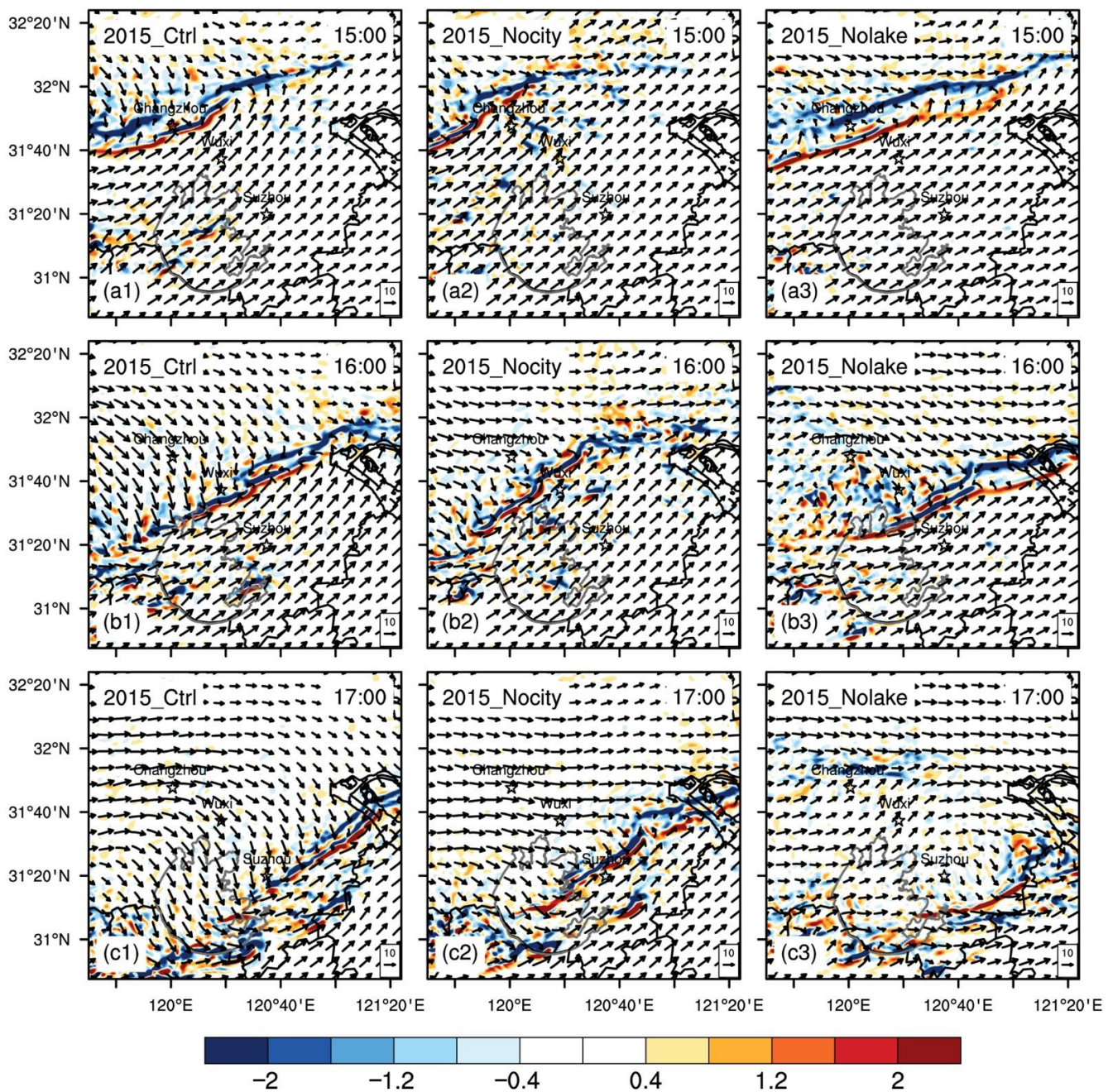


Figure 11. The spatial distributions of the 850 hPa wind direction and divergence (unit: 10^{-3} s^{-1}) for the (a1,b1,c1) control, (a2,b2,c2) Nocity, (a3,b3,c3) Nolake runs for EP627.

The moving direction of the 850 hPa shear line in Nocity is consistent with the control run (Figure 11a2,b2,c2). The intensity and position at 15:00 are similar to those of the control run, but the moving speed is significantly slower for the next two times and the location is more northwest. However, the intensity changes little and does not intensify and weaken as markedly as in the control run. The corresponding SCL shows an intensifying trend (Figure 8a2,b2,c2), and the position is similar to the 850 hPa shear line, but its intensity is clearly weaker than in the control run. The moving direction of the 850 hPa shear line in Nolake is also consistent with the control run (Figure 11a3,b3,c3). The intensity of the 850 hPa shear line at 15:00 is close to the control run, but it is significantly weakened in the next two times, and at 17:00 it is almost dissipated. The intensity of the corresponding SCL does not change much (Figure 8a3,b3,c3); its position is more southeast than the 850 hPa shear line, but its intensity is evidently weaker than in the control run, and the SCL in Lake Taihu at 17:00 has clearly dissipated.

It is worth noting that the 850 hPa shear line has discontinuous fractures at 15:00 and 17:00, which occurs in Changzhou at 15:00 and at the southeastern edge of Lake Taihu at 17:00. By combining the profile (Figure 9a1) and the movement of the SCL (Figure 8a1,c1), it is known that convergence of strong near-surface wind near SXCMA and Lake Taihu will form strong vertical movement from the surface to the low level, further affecting the flow field of the pressure layer where the LLSL is located and causing the LLSL to break.

For a better attention to the changes of water vapor in the lower layer within the study area during the movement of the shear line, a 1000–850 hPa water vapor flux integration is introduced to show the distribution of water vapor in the lower layer. In the control run, along with the movement of the shear line, large water vapor flux centers (Figure 12a1,b1,c1) will be generated on both sides of the shear line, and some large value centers are located in the areas where SXCMA and Lake Taihu are located. Especially at 17:00, the range and intensity of the large value center of water vapor flux above Lake Taihu, where the shear line is located, is the most distinct. For Nocity, although there is also a large water vapor flux near the shear line, the range and intensity of the large value distribution are clearly weaker than in the control run (Figure 12a2,b2,c2), which is mostly related to the weaker shear line. The intensity and range of the large water vapor flux in Nolake is far inferior to that of the control run (Figure 12a3,b3,c3), which is evidently related to the lack of Lake Taihu, leading to less water vapor supply in the lower levels and a weaker shear line than the control run. More precisely, with or without Lake Taihu, the water vapor flux differences around the lake in the lower levels can range from 50 to 400 kg m⁻¹ s⁻¹ (Figure 12a4,b4,c4).

3.4.2. EP925

In EP925, the characteristics of the LLSL of 925 hPa are more obvious than that of 850 hPa. Therefore, the shift of the 925 hPa shear line in the study area is chosen to explore the impact of metropolises and lakes on the LLSL. In the control run, the 925 hPa shear line gradually moves from southern Changzhou to Wuxi with little enhancement (Figure 13a1,b1) and develops into a low vortex when moving to Suzhou (Figure 13c1). Corresponding to the shear line position, there has always been a strong SCL on the ground (Figure 10a1,b1,c1). For Nocity, no conspicuous shear line is generated at 925 hPa (Figure 13a2,b2,c2), and no strong SCL is generated on the corresponding ground (Figure 10a2,b2,c2). The 925 hPa shear line of Nolake is more distinct only in Changzhou (Figure 13a3), and the other two times are weaker and less visible (Figure 13b3,c3). Although the corresponding SCL exists, its intensity is not as strong as in the control run (Figure 10a3,b3,c3).

In terms of the distribution of water vapor in the low level, marked large water vapor fluxes near metropolises and lakes formed accompanied by the movement of the shear line in the control run (Figure 14a1,b1,c1). For Nocity, because no conspicuous shear line occurs, there is no large water vapor flux (Figure 14a2,b2,c2). A large value center of water vapor flux exists in Nolake (Figure 14a3,b3,c3), but its intensity and range are obviously

inferior to the control run. This is evidently related to the loss of Lake Taihu, which leads to a decrease in water vapor in the lower level and in the intensity of the shear line. More specifically, with Lake Taihu, the control run produces 50 to 150 kg m⁻¹ s⁻¹ more water vapor flux around the lake in the lower levels than Nolake (Figure 14a4,b4,c4).

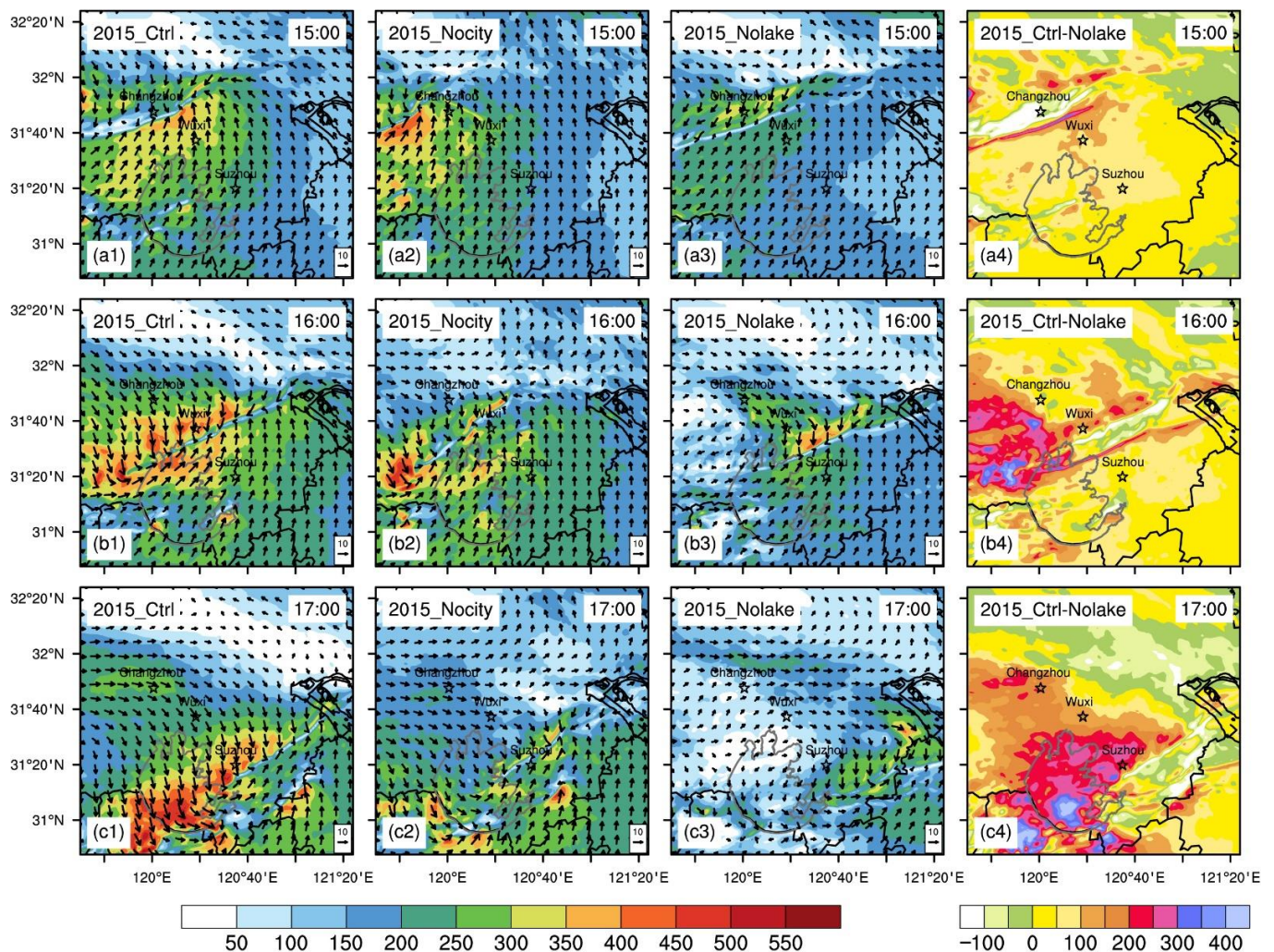


Figure 12. The spatial distributions of the water vapor fluxes (shaded, unit: kg m⁻¹ s⁻¹) integrated from 1000 hPa to 850 hPa and the mean horizontal wind directions (arrows, unit: m s⁻¹) for the (a1,b1,c1) control, (a2,b2,c2) Nocity, (a3,b3,c3) Nolake runs, and (a4,b4,c4) the difference of water vapor fluxes between the control and Nolake runs for EP627.

3.5. Mechanism of Metropolises and Lakes Impacts on the Shear Line Torrential Rain

Through the analysis of the simulation results of EP627 and EP925, we can summarize the impact mechanisms of metropolitan areas and shallow lakes in the process of shear line heavy rain as the following: Metropolises and lakes affect the SKT through their special surface properties. Especially for metropolises, the SKT is significantly higher than the surrounding environment in the daytime. When the LLSL passes, a strong SCL corresponding to the shear line is generated. The strong vertical convective motion generated by the strong SCL interacts with the LLSL to intensify each other and ensure that the LLSL is maintained or intensified during the movement.

In addition, we compared the shape and intensity of the LLSL while they are born near the study area until the time before they intrude into the study area in the control and two sensitivity runs of the two cases (figure omitted). It is found that the presence or absence of a city has a significantly greater impact on the intensity and shape of the LLSL

near the city than near the lake. The LLSL generated northwest of Changzhou is weaker when there is no city, while when there is no Lake Taihu, the intensity and shape of the LLSL are not much different from the control run.

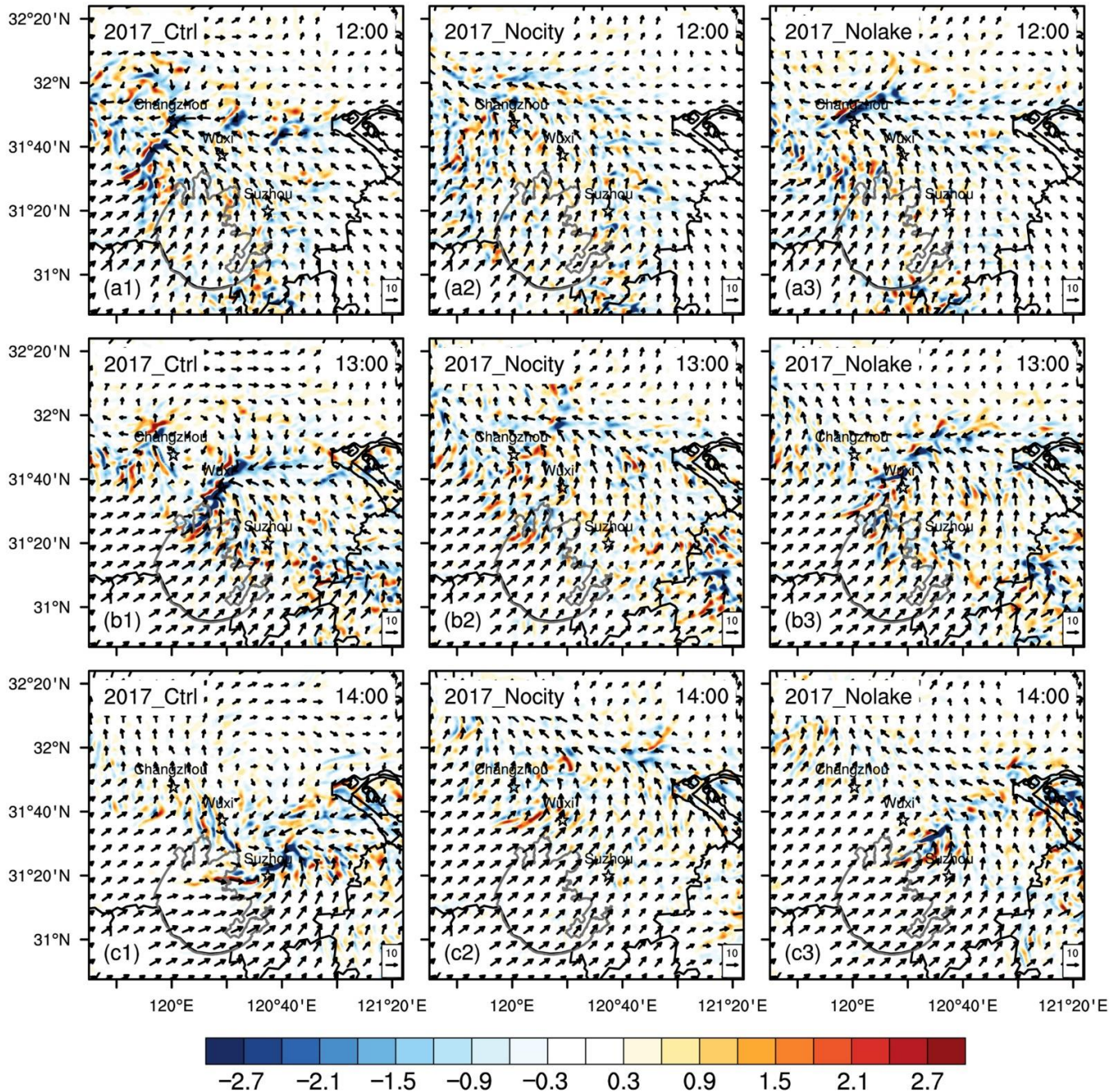


Figure 13. The spatial distributions of the 925 hPa wind direction and divergence (unit: 10^{-3} s^{-1}) for the (a1,b1,c1) control, (a2,b2,c2) Nocity, (a3,b3,c3) Nolake runs for EP925.

A lake, through the lake–land breeze effect and its lower surface roughness, has an impact on the intensity and movement of the SCL, and will trigger strong ground convection around the lake under appropriate conditions. This can indirectly adjust and affect the shear line rainfall belt position, and as source of water vapor, it will directly increase the intensity of precipitation for the supply of low-level water vapor to the surrounding environment.

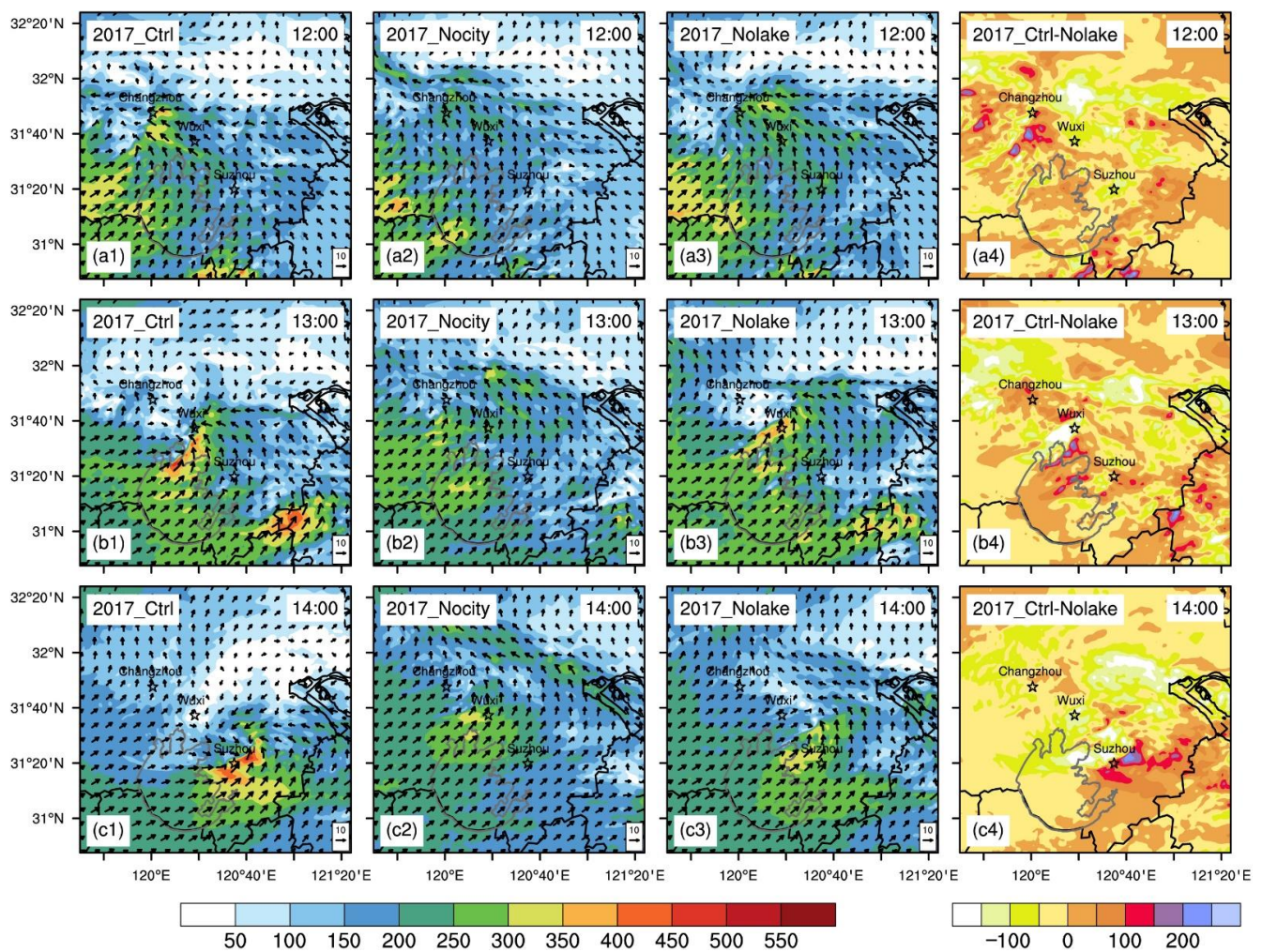


Figure 14. The spatial distributions of the water vapor fluxes (shaded, unit: $\text{kg m}^{-1} \text{s}^{-1}$) integrated from 1000 hPa to 850 hPa and the mean horizontal wind directions (arrows, unit: m s^{-1}) for the (a1,b1,c1) control, (a2,b2,c2) Nocity, (a3,b3,c3) Nolake runs, and (a4,b4,c4) the difference of water vapor fluxes between the control and Nolake runs for EP925.

It is worth noting that in EP627, when the temperature difference between the metropolises and the surrounding environment was large, the SCL was strong, and the position of the SCL was quite different from the LLSL. The strong vertical convection formed by the SCL can extend to the pressure layer where the LLSL is located and causes the shear line to discontinuously break over the urban area, resulting in a change in the location of the precipitation.

4. Conclusions and Discussion

This study simulated the two extreme precipitation events of EP627 and EP925 caused by LLSL using a WRF model at 1 km high-resolution. Two sensitivity runs are conducted and explore the relative impacts of Lake Taihu and SXCMA on shear line extreme precipitation when compared with the control run. The main conclusions are as follows:

- (1) Under the interaction of Lake Taihu and SXCMA, the precipitation in the study area will increase significantly. The simulation results in EP627 show that the SXCMA and Taihu Lake have increased precipitation by 10.6% and 5.8%, respectively, while for EP925 the numbers are 15.9% and 7.3%, which means that the influence of Lake Taihu and SXCMA on stronger shear line precipitation (EP627) is significantly weaker than

that of a strong shear line (EP925). In addition, the SXCMA has a more obvious effect on enhancing precipitation—about twice that of Lake Taihu.

- (2) SXCMA mainly affects the intensity and movement of the SCL in the study area, and the strong vertical convection formed through the SCL will interact with the LLSL and indirectly affect the intensity and movement of the LLSL. This, in turn, affects the intensity and location of precipitation. SXCMA will markedly affect the generation intensity and shape of the LLSLs near the study area, and the impact of SXCMA on the LLSLs is significantly greater than that of Lake Taihu, as in EP925, Nocity did not produce distinct shear lines in the low level.
- (3) Lake Taihu plays an important role in maintaining the SCL during its movement due to lower surface roughness and lake–land breeze. Under the strong lake–land temperature difference, strong vertical convection on the ground will be triggered around Taihu Lake, then adjust and affect the location and intensity of the LLSL precipitation. In addition, Lake Taihu’s supply of water vapor to its surroundings will intensify the precipitation in the study area.

This paper explores the impact of Lake Taihu and the surrounding metropolitan area on the shear line torrential rain process in Eastern China. Although some discoveries have been made, there are also some shortcomings. For example, the specific impact mechanism of the metropolis on the surrounding LLSL generation process is still unclear, so further exploration and analysis are needed. In addition, the conclusion of this article is based on the study of two events. To obtain a more reliable conclusion, more typical cases may need to be added.

Author Contributions: Conceptualization, Y.G.; methodology, Z.L. and Y.G.; software, Z.L.; validation, Z.L.; formal analysis, Z.L.; investigation, Z.L.; resources, Y.G.; data curation, Z.L.; writing—original draft, Z.L.; writing—review and editing, Z.L. and Y.G.; visualization, Z.L.; supervision, Y.G.; project administration, Y.G.; funding acquisition, Y.G. All authors have read and agreed to the published version of the manuscript.

Funding: This research was funded by the National Key Research and Development Program of China (2017YFC1502101).

Institutional Review Board Statement: Not applicable.

Informed Consent Statement: Not applicable.

Data Availability Statement: Not applicable.

Acknowledgments: The support of the Fudan University–Tibet University Joint Laboratory for Biodiversity and Global Change and Shanghai Frontiers Science Center of Atmosphere–Ocean Interaction, are appreciated. Yanhong Gao is involved in the CORDEX-FPS-CPTP. We thank the China Meteorological Data Service Centre for providing the station data and the Merged data set, the Jiangsu province Meteorological Bureau for the S-band raw radar data of CINRAD-SA Doppler weather radar, the NASA/Goddard Space Flight Center for the GPM data, and the ECMWF for the free access to the ERA-Interim Reanalysis data set. The work was carried out at the National Supercomputer Center in Tianjin.

Conflicts of Interest: The authors declare no conflict of interest.

References

1. United Nations, Department of Economic and Social Affairs, Population Division. *World Urbanization Prospects: The 2018 Revision (ST/ESA/SER. A/420)*; United Nations: New York, NY, USA, 2019; pp. 9–55.
2. Miao, S.; Chen, F.; Li, Q.; Fan, S. Impacts of Urban Processes and Urbanization on Summer Precipitation: A Case Study of Heavy Rainfall in Beijing on 1 August 2006. *J. Appl. Meteorol. Climatol.* **2011**, *50*, 806–825. [[CrossRef](#)]
3. Wang, J.; Feng, J.; Yan, Z.; Hu, Y.; Jia, G. Nested high-resolution modeling of the impact of urbanization on regional climate in three vast urban agglomerations in China. *J. Geophys. Res. Atmos.* **2012**, *117*, D21103. [[CrossRef](#)]
4. Dou, J.; Wang, Y.; Bornstein, R.; Miao, S. Observed spatial characteristics of Beijing urban climate impacts on summer thunderstorms. *J. Appl. Meteorol. Climatol.* **2015**, *54*, 94–105. [[CrossRef](#)]

5. Debbage, N.; Shepherd, J.M. Urban influences on the spatiotemporal characteristics of runoff and precipitation during the 2009 Atlanta flood. *J. Hydrometeorol.* **2019**, *20*, 3–21. [[CrossRef](#)]
6. Zhang, D.-L. Rapid urbanization and more extreme rainfall events. *Sci. Bull.* **2020**, *65*, 516–518. [[CrossRef](#)]
7. Shepherd, J.M.; Burian, S.J. Detection of urban-induced rainfall anomalies in a major coastal city. *Earth Interact.* **2003**, *7*, 1–17. [[CrossRef](#)]
8. Thielen, J.; Wobrock, W.; Gadian, A.; Mestayer, P.; Creutin, J.-D. The possible influence of urban surfaces on rainfall development: A sensitivity study in 2D in the meso- γ -scale. *Atmos. Res.* **2000**, *54*, 15–39. [[CrossRef](#)]
9. Bornstein, R.; Lin, Q. Urban heat islands and summertime convective thunderstorms in Atlanta: Three case studies. *Atmos. Environ.* **2000**, *34*, 507–516. [[CrossRef](#)]
10. Diem, J.E.; Brown, D.P. Anthropogenic impacts on summer precipitation in central Arizona, USA. *Prof. Geogr.* **2003**, *55*, 343–355.
11. Schmid, P.E.; Niyogi, D. Modeling urban precipitation modification by spatially heterogeneous aerosols. *J. Appl. Meteorol. Climatol.* **2017**, *56*, 2141–2153. [[CrossRef](#)]
12. Huang, A.; Wang, J.; Dai, Y.; Yang, K.; Wei, N.; Wen, L.; Wu, Y.; Zhu, X.; Zhang, X.; Cai, S. Evaluating and improving the performance of three 1-D Lake models in a large deep Lake of the central Tibetan Plateau. *J. Geophys. Res. Atmos.* **2019**, *124*, 3143–3167. [[CrossRef](#)] [[PubMed](#)]
13. Farley Nicholls, J.; Toumi, R. On the lake effects of the Caspian Sea. *Q. J. R. Meteorol. Soc.* **2014**, *140*, 1399–1408. [[CrossRef](#)]
14. Sun, X.; Xie, L.; Semazzi, F.; Liu, B. Effect of lake surface temperature on the spatial distribution and intensity of the precipitation over the Lake Victoria basin. *Mon. Weather. Rev.* **2015**, *143*, 1179–1192. [[CrossRef](#)]
15. Tsujimoto, K.; Koike, T. Land-lake breezes at low latitudes: The case of Tonle Sap Lake in Cambodia. *J. Geophys. Res. Atmos.* **2013**, *118*, 6970–6980. [[CrossRef](#)]
16. Ma, Y.; Yang, Y.; Qiu, C.; Wang, C. Evaluation of the WRF-lake model over two major freshwater lakes in China. *J. Meteorol. Res.* **2019**, *33*, 219–235. [[CrossRef](#)]
17. Eichenlaub, V.L. Lake effect snowfall to the lee of the Great Lakes: Its role in Michigan. *Bull. Am. Meteorol. Soc.* **1970**, *51*, 403–413. [[CrossRef](#)]
18. Notaro, M.; Holman, K.; Zarrin, A.; Fluck, E.; Vavrus, S.; Bennington, V. Influence of the Laurentian Great Lakes on regional climate. *J. Clim.* **2013**, *26*, 789–804. [[CrossRef](#)]
19. Dai, Y.; Wang, L.; Yao, T.; Li, X.; Zhu, L.; Zhang, X. Observed and simulated lake effect precipitation over the Tibetan Plateau: An initial study at Nam Co Lake. *J. Geophys. Res. Atmos.* **2018**, *123*, 6746–6759. [[CrossRef](#)]
20. Wen, L.; Lv, S.; Li, Z.; Zhao, L.; Nagabhatla, N. Impacts of the Two Biggest Lakes on Local Temperature and Precipitation in the Yellow River Source Region of the Tibetan Plateau. *Adv. Meteorol.* **2015**, *2015*, 248031. [[CrossRef](#)]
21. Laird, N.F.; Desrochers, J.; Payer, M. Climatology of lake-effect precipitation events over Lake Champlain. *J. Appl. Meteorol. Climatol.* **2009**, *48*, 232–250. [[CrossRef](#)]
22. Alcott, T.I.; Steenburgh, W.J.; Laird, N.F. Great Salt Lake-effect precipitation: Observed frequency, characteristics, and associated environmental factors. *Weather. Forecast.* **2012**, *27*, 954–971. [[CrossRef](#)]
23. Owens, N.D.; Rauber, R.M.; Jewett, B.F.; McFarquhar, G.M. The contribution of lake enhancement to extreme snowfall within the Chicago–Milwaukee urban corridor during the 2011 Groundhog Day blizzard. *Mon. Weather. Rev.* **2017**, *145*, 2405–2420. [[CrossRef](#)]
24. Zou, H.; Zhang, S.; Liu, Y.; Zhang, W.; Yang, X. Analysis of a Convective Storm Crossing Poyang Lake in China. *J. Meteorol. Res.* **2020**, *34*, 529–545. [[CrossRef](#)]
25. Schroeder, J.J.; Kristovich, D.A.; Hjelmfelt, M.R. Boundary layer and microphysical influences of natural cloud seeding on a lake-effect snowstorm. *Mon. Weather. Rev.* **2006**, *134*, 1842–1858. [[CrossRef](#)]
26. Keeler, J.M.; Kristovich, D.A. Observations of urban heat island influence on lake-breeze frontal movement. *J. Appl. Meteorol. Climatol.* **2012**, *51*, 702–710. [[CrossRef](#)]
27. Yang, L.; Smith, J.A.; Baeck, M.L.; Bou-Zeid, E.; Jessup, S.M.; Tian, F.; Hu, H. Impact of Urbanization on Heavy Convective Precipitation under Strong Large-Scale Forcing: A Case Study over the Milwaukee–Lake Michigan Region. *J. Hydrometeorol.* **2014**, *15*, 261–278. [[CrossRef](#)]
28. Lee, X.; Liu, S.; Xiao, W.; Wang, W.; Gao, Z.; Cao, C.; Hu, C.; Hu, Z.; Shen, S.; Wang, Y.; et al. The Taihu Eddy Flux Network: An Observational Program on Energy, Water, and Greenhouse Gas Fluxes of a Large Freshwater Lake. *Bull. Am. Meteorol. Soc.* **2014**, *95*, 1583–1594. [[CrossRef](#)]
29. Jiangsu Provincial Bureau of Statistics; Survey Office of the National Bureau of Statistics in Jiangsu. *Jiangsu Statistical Yearbook*; China Statistics Press: Beijing, China, 2019; pp. 35–75.
30. Gu, H.; Ma, Z.; Li, M. Effect of a large and very shallow lake on local summer precipitation over the Lake Taihu basin in China. *J. Geophys. Res. Atmos.* **2016**, *121*, 8832–8848. [[CrossRef](#)]
31. Wang, Y.; Gao, Y.; Qin, H.; Huang, J.; Liu, C.; Hu, C.; Wang, W.; Liu, S.; Lee, X. Spatiotemporal Characteristics of Lake Breezes over Lake Taihu, China. *J. Appl. Meteorol. Climatol.* **2017**, *56*, 2053–2065. [[CrossRef](#)]
32. Zhang, X.; Huang, J.; Li, G.; Wang, Y.; Liu, C.; Zhao, K.; Tao, X.; Hu, X.-M.; Lee, X. Improving Lake-Breeze Simulation with WRF Nested LES and Lake Model over a Large Shallow Lake. *J. Appl. Meteorol. Climatol.* **2019**, *58*, 1689–1708. [[CrossRef](#)]
33. Donat, M.G.; Lowry, A.L.; Alexander, L.V.; O’Gorman, P.A.; Maher, N. More extreme precipitation in the world’s dry and wet regions. *Nat. Clim. Change* **2016**, *6*, 508–513. [[CrossRef](#)]

34. Zhang, W.; Zhou, T. Increasing impacts from extreme precipitation on population over China with global warming. *Sci. Bull.* **2020**, *65*, 243–252. [[CrossRef](#)]
35. Liu, R.; Liu, S.C.; Cicerone, R.J.; Shiu, C.-J.; Li, J.; Wang, J.; Zhang, Y. Trends of extreme precipitation in eastern China and their possible causes. *Adv. Atmos. Sci.* **2015**, *32*, 1027–1037. [[CrossRef](#)]
36. Yu, R.; Li, J.; Yuan, W.; Chen, H. Changes in characteristics of late-summer precipitation over eastern China in the past 40 years revealed by hourly precipitation data. *J. Clim.* **2010**, *23*, 3390–3396. [[CrossRef](#)]
37. Zhai, P.; Zhang, X.; Wan, H.; Pan, X. Trends in total precipitation and frequency of daily precipitation extremes over China. *J. Clim.* **2005**, *18*, 1096–1108. [[CrossRef](#)]
38. Zhang, Q.; Zheng, Y.; Singh, V.P.; Luo, M.; Xie, Z. Summer extreme precipitation in eastern China: Mechanisms and impacts. *J. Geophys. Res. Atmos.* **2017**, *122*, 2766–2778. [[CrossRef](#)]
39. Chen, Y.; Zhai, P. Precursor circulation features for persistent extreme precipitation in central-eastern China. *Weather. Forecast.* **2014**, *29*, 226–240. [[CrossRef](#)]
40. Luo, Y.; Wu, M.; Ren, F.; Li, J.; Wong, W.-K. Synoptic situations of extreme hourly precipitation over China. *J. Clim.* **2016**, *29*, 8703–8719. [[CrossRef](#)]
41. Tang, Y.; Huang, A.; Wu, P.; Huang, D.; Xue, D.; Wu, Y. Drivers of summer extreme precipitation events over East China. *Geophys. Res. Lett.* **2021**, e2021GL093670. [[CrossRef](#)]
42. Gao, T.; Xie, L. Spatiotemporal changes in precipitation extremes over Yangtze River basin, China, considering the rainfall shift in the late 1970s. *Glob. Planet. Change* **2016**, *147*, 106–124. [[CrossRef](#)]
43. Kang, C.; Luo, Z.; Zong, W.; Hua, J. Impacts of Urbanization on Variations of Extreme Precipitation over the Yangtze River Delta. *Water* **2021**, *13*, 150. [[CrossRef](#)]
44. Ma, J.; Yao, X. Statistical analysis of the shear lines and torrential rains over the Yangtze-Huaihe river region during June–July in 1981–2013. *Acta Meteorol. Sin.* **2015**, *73*, 883–894.
45. Gao, Y.; Xue, Y.; Peng, W.; Kang, H.-S.; Waliser, D. Assessment of dynamic downscaling of the extreme rainfall over East Asia using a regional climate model. *Adv. Atmos. Sci.* **2011**, *28*, 1077–1098. [[CrossRef](#)]
46. Skamarock, W.C.; Klemp, J.B.; Dudhia, J.; Gill, D.O.; Barker, D.M.; Duda, M.G.; Huang, X.-Y.; Wang, W.; Powers, J.G. *A Description of the Advanced Research WRF Version 3*; National Center for Atmospheric Research: Boulder, CO, USA, 2008; pp. 142–163.
47. Wang, Z.; Duan, A.; Wu, G. Impacts of boundary layer parameterization schemes and air-sea coupling on WRF simulation of the East Asian summer monsoon. *Sci. China Earth Sci.* **2014**, *57*, 1480–1493. [[CrossRef](#)]
48. Wang, H.; Jiang, Y.; Chen, Z.; Chen, J. Numerical Simulation and Diagnostic Analysis of a Yangtze and Huaihe River Shear-line Heavy Rainfall Event. *Meteorol. Environ. Sci.* **2012**, *35*, 17–25.
49. Liu, R.; Ding, Z.; Zhang, Y.; Ma, C. Numerical simulation on a MCV case in Yangtze-Huaihe Basin. *J. Meteorol. Sci.* **2018**, *38*, 46–56.
50. Zhang, Y.; Zhang, F.; Davis, C.A.; Sun, J. Diurnal evolution and structure of long-lived mesoscale convective vortices along the Mei-Yu front over the East China Plains. *J. Atmos. Sci.* **2018**, *75*, 1005–1025. [[CrossRef](#)]
51. Wang, R.; Zhu, Y.; Qiao, F.; Liang, X.-Z.; Zhang, H.; Ding, Y. High-resolution Simulation of an Extreme Heavy Rainfall Event in Shanghai Using the Weather Research and Forecasting Model: Sensitivity to Planetary Boundary Layer Parameterization. *Adv. Atmos. Sci.* **2021**, *38*, 98–115. [[CrossRef](#)]
52. Gu, H.; Jin, J.; Wu, Y.; Ek, M.B.; Subin, Z.M. Calibration and validation of lake surface temperature simulations with the coupled WRF-lake model. *Clim. Change* **2015**, *129*, 471–483. [[CrossRef](#)]
53. Shen, Y.; Zhao, P.; Pan, Y.; Yu, J. A high spatiotemporal gauge-satellite merged precipitation analysis over China. *J. Geophys. Res. Atmos.* **2014**, *119*, 3063–3075. [[CrossRef](#)]
54. Huffman, G.J.; Bolvin, D.T.; Braithwaite, D.; Hsu, K.; Joyce, R.; Xie, P.; Yoo, S.-H. NASA global precipitation measurement (GPM) integrated multi-satellite retrievals for GPM (IMERG). *Algorithm Theor. Basis Doc. (ATBD) Version* **2015**, *4*, 26.
55. Yu, L.; Leng, G.; Python, A.; Peng, J. A Comprehensive Evaluation of Latest GPM IMERG V06 Early, Late and Final Precipitation Products across China. *Remote Sens.* **2021**, *13*, 1208. [[CrossRef](#)]
56. Zhou, C.; Gao, W.; Hu, J.; Du, L.; Du, L. Capability of IMERG V6 Early, Late, and Final Precipitation Products for Monitoring Extreme Precipitation Events. *Remote Sens.* **2021**, *13*, 689. [[CrossRef](#)]
57. Wilks, D.S. *Statistical Methods in the Atmospheric Sciences*, 3rd ed.; Elsevier: Amsterdam, The Netherlands, 2011; pp. 306–315.